Chapter 5
Calculation of Images of Thin Specimens

Abstract This chapter presents approximate methods of calculating transmission electron microscope images of thin specimens. The thickness of the specimen is ignored, which may be appropriate for very thin specimens. Multiple scattering is also generally ignored. This approach is intermediate between the transfer function (in previous chapters) and the multislice and Bloch wave methods (discussed in later chapters) and has the advantage of requiring much less computer time.

This chapter discusses the calculation of an electron microscope image neglecting the geometrical thickness of the specimen (i.e., very thin specimens). Many practical specimens are too thick for this type of calculation to be quantitatively correct. However, this approach can provide a qualitative insight into the structure in the image and it requires much less computer time. This type of image simulation is sometimes referred to as a phase grating approximation or a kinematical image approximation because it does not properly include the effects of multiple or plural scattering within the specimen. Calculation of the transmission function of thin specimens is also a necessary part of more advanced calculations including a realistic specimen thickness that will be considered in later chapters. In particular the calculation presented in this chapter will form a single slice of the multislice algorithm.

The kinetic energy of the imaging electrons in the electron microscope approaches their rest mass energy. A detailed quantum mechanical calculation of the motion of these electrons should properly be calculated using relativistic quantum mechanics (the Dirac equation with spin). As discussed in Sect. 2.3 the relativistic effects can be approximated by using the nonrelativistic Schrödinger equation (neglecting electron spin) with the relativistically correct wavelength and mass of the electron. This approximation is probably accurate enough at 100 keV but may be less accurate at 1 MeV. Nonrelativistic quantum mechanics is however dramatically easier to work with, and this approximation will be used here.

E.J. Kirkland, *Advanced Computing in Electron Microscopy*,
DOI 10.1007/978-1-4419-6533-2_5,

5.1 The Weak Phase Object

The primary interaction between the specimen and the imaging electrons is between the electrostatic potential of the specimen and the charge on the electron. The electrons traveling down the column of the microscope (before hitting the specimen) are a superposition of one or more plane waves. In the CTEM the incident electrons are primarily in a single plane wave and the STEM probe is a superposition of many plane waves (i.e., a spherically convergent probe). It suffices to consider the effect of the specimen on one plane wave. The wave function ψ for one plane wave traveling along the optic axis in the z direction is:

$$\psi(\mathbf{x}) = \exp(2\pi \mathrm{i} k_z z) = \exp(2\pi \mathrm{i} z/\lambda), \tag{5.1}$$

where λ is the wavelength of the electron and $k_z = 1/\lambda$ is the propagation wave vector. The relativistic expression for the reciprocal of the electron wavelength in vacuum [see (2.5)] is:

$$k_z = \frac{1}{\lambda} = \frac{\sqrt{eV(2m_0c^2 + eV)}}{hc}, \tag{5.2}$$

where m_0 is the rest mass of the electron, c the speed of light in vacuum, h Planck's constant, and eV is the kinetic energy of the electron in vacuum.

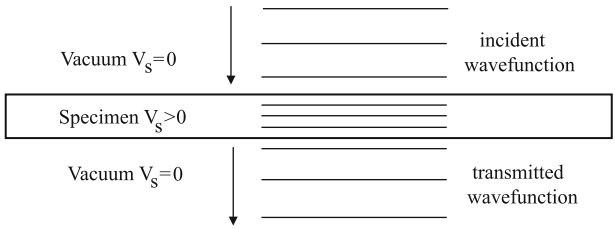

Fig. 5.1 An incident (high energy) electron plane wave passing through the electrostatic potential V_s of the specimen. The wave function is drawn as lines of constant phase, and the specimen is assumed to have a uniform constant potential. The electron wavelength is reduced by the positive potential inside the specimen. This drawing is not to scale

The imaging electrons typically have a much higher energy than the electrons in the specimen. If the specimen is thin the imaging electrons pass through the specimen with only a small deviation in their path. This deviation can be approximated as a small change in wavelength of the electrons as they pass through the specimen (see Fig. 5.1). The specimen has a small electrostatic potential which influences the electron wavelength. If the potential inside the specimen is positive then the imaging electrons are accelerated inside the specimen giving them a smaller wavelength. If eV_s is the additional electrostatic potential energy of the imaging

electrons while in the specimen and λ_s is their wavelength then while inside the specimen:

$$\begin{aligned}\frac{1}{\lambda_s} &= \frac{[(eV+eV_s)(2m_0c^2+eV+eV_s)]^{1/2}}{hc} \\ &= \frac{[eV(2m_0c^2+eV)+eV_s(2m_0c^2+2eV+eV_s)]^{1/2}}{hc} \\ &= \frac{1}{\lambda}\left[1+\frac{eV_s(2m_0c^2+2eV+eV_s)}{eV(2m_0c^2+eV)}\right]^{1/2}. \end{aligned} \tag{5.3}$$

Expanding this equation and keeping only the lowest order terms in V_s/V yields:

$$\begin{aligned}\frac{1}{\lambda_s} &\sim \frac{1}{\lambda}\left[1+\frac{eV_s(2m_0c^2+2eV)}{2eV(2m_0c^2+eV)}+\cdots\right] \\ &\sim k_z+\frac{V_s(m_0c^2+eV)}{\lambda V(2m_0c^2+eV)}+\cdots \end{aligned} \tag{5.4}$$

Changing the wavelength is equivalent to shifting the phase of the electron as it passes through the specimen (i.e., changing the wave vector k_z). Therefore, the electron wave function while passing through the specimen is:

$$\psi(\mathbf{x}) \sim \exp(2\pi \mathrm{i} k_z z)\exp(i\sigma V_s z), \tag{5.5}$$

where the interaction parameter σ is:

$$\sigma = \frac{2\pi}{\lambda V}\left(\frac{m_0c^2+eV}{2m_0c^2+eV}\right) = \frac{2\pi m e\lambda}{h^2} \tag{5.6}$$

$m=\gamma m_0$ is the relativistic mass. This expression assumes that the specimen potential V_s is much smaller than the beam energy ($V_s/V \ll 1$). Also remember that the specimen potential varies with position although not explicitly written earlier. It is traditional to use the same symbol for both the interaction parameter and the scattering cross section, but the meaning should usually be clear from the context in which each is used. The interaction parameter is plotted vs. the electron kinetic energy in Fig. 5.2. The interaction parameter decreases rapidly with increasing electron energy at low electron energy but is nearly constant for electron energies above about 300 keV.

If the specimen is very thin then the electron wave function accumulates a total phase change while passing through the specimen that is just the integral of the potential of the specimen. The incident electrons pass through the specimen and the effect of the specimen is to multiply the incident wave function (5.1) by the specimen transmission function $t(\mathbf{x})$. The wave function transmitted through the specimen is:

$$\begin{aligned}\psi_t(\mathbf{x}) &= t(\mathbf{x})\exp(2\pi \mathrm{i} k_z z) \\ t(\mathbf{x}) &= \exp[\mathrm{i}\sigma v_z(\mathbf{x})] \end{aligned} \tag{5.7}$$

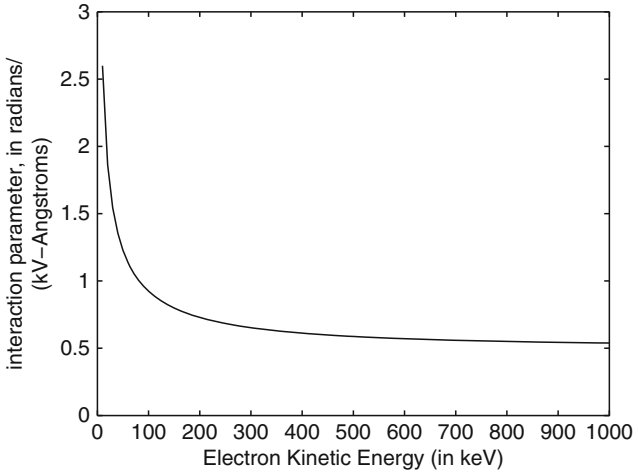

Fig. 5.2 The interaction parameter σ vs. the electron kinetic energy

and the projected atomic potential $v_z(\mathbf{x})$ is the integral along the optic axis, z of the specimen:

$$v_z(\mathbf{x}) = v_z(x,y) = \int V_s(x,y,z)\mathrm{d}z \tag{5.8}$$

This is the so-called weak phase object approximation (Cowley and Iijima [62]). There are really two assumptions in this approximation. One is that the potential inside the specimen is very small and the other is that the accumulated effect of the specimen can be replaced with a simple integral along z.

5.2 Single Atom Properties

Single atoms are a reasonable starting point to discuss the simulation of electron microscope images in the weak phase object approximation. Single isolated atoms with low to medium atomic number satisfy the thin specimen requirement and can actually be seen in some microscopes under the appropriate conditions. Furthermore the potential and charge distribution of single atoms can be calculated from first principles using relativistic Hartree-Fock theory in a reasonably well defined although tedious manner. To find the potential and charge distribution in a single atom requires finding the wave function of all electrons in the atom (to a good approximation the atomic nucleus may be regarded as a fixed point charge at the origin). Hydrogen is the only atom which can be solved analytically and a derivation is usually given in most quantum mechanics text books (see for example Eisberg [88] or Schiff [312]). Unfortunately, atoms with more than one electron (that is, the rest of the periodic chart) must be solved numerically with some approximations. The Hartree-Fock method forms an effective many-electron wave function obeying

the Pauli exclusion principle that also satisfies the Schrödinger wave equation (or in the case of the relativistic Hartree-Fock method the Dirac wave equation). The method reduces to repeatedly solving a single particle wave equation for each electron orbital that is moving in an effective potential due to the charge on the nucleus and the average interactions with all other electrons in the atoms. Each electron orbital is calculated using the current distribution of the other electrons in the atoms and the process is repeated for all orbitals until the electron wave functions for all electrons converge to a final self-consistent result. Relativistic effects are probably negligible for low atomic numbers (like carbon) but are significant for high atomic numbers (like gold) because the core electrons near the nucleus experience a very large electric field and have a large kinetic energy (i.e., velocity). A detailed discussion of the Hartree-Fock method is beyond the scope of this book but may be found in the books by Froese-Fischer [117], Szasz [339] and Froese-Fischer et al. [106]. Appendix C gives a detailed description of using a relativistic Hartree-Fock program to calculate a complete set of atomic potentials for the whole periodic chart (atomic number $Z = 2$ through $Z = 103$).

5.2.1 Radial Charge Distribution

The radial electron charge distribution $\rho(r)$ of each atom is generated as part of the Hartree-Fock atomic structure calculation. The calculated radial charge distribution for a few selected atoms is shown in Fig. 5.3. The peaks in the charge distribution correspond to the atomic orbitals (or electron shells) of each atom. It is interesting to note that although the total number of electrons increases with atomic number Z the actual size of the atoms does not change dramatically with atomic number. The increasing charge of the nucleus (with increasing Z) causes the electrons to be attracted more strongly to the nucleus roughly keeping the actual atomic size relatively constant at about one Angstrom in diameter.

5.2.2 Potential

The atomic potential is a more interesting quantity for electron microscopy because the imaging electrons in the microscope interact directly with the atomic potential [see (5.5)]. The charge distribution and potential are related via Poisson's equation from electromagnetic theory. The Mott-Bethe [25, 27, 255, 256] formula (C.7) is equivalent to Poisson's equation, however it is stated in reciprocal space. Figure 5.3 only includes the electron charge distribution, however the large point charge on the atomic nucleus probably has the strongest interaction with the imaging electrons. The electron cloud in Fig. 5.3 mainly serves to shield the atomic nucleus (remember that the nucleus has a positive charge but the electron cloud has a negative charge). When the charge on the atomic nucleus is added to the atomic electron charge

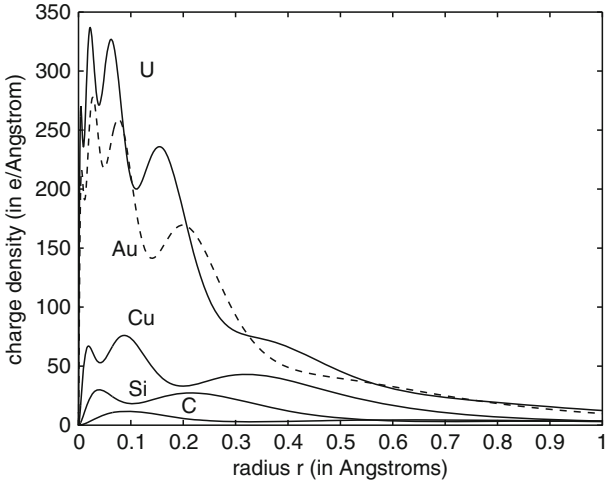

Fig. 5.3 The calculated electron charge distribution $4\pi r^2\rho(r)$ (in electrons per Å) for isolated single atoms at the origin vs. the three dimensional radius r. The atoms are carbon (Z6), silicon (Z = 14), copper (Z = 29), gold (Z = 79), and uranium (Z = 92)

distribution and the resulting charge distribution is transformed into an atomic potential the total potential is much more strongly peaked near the nucleus (at the origin). The Hartree-Fock procedure of necessity ends up with a large table of numbers. Appendix C details how to parameterize the tabulated Hartree-Fock results. To a reasonably good approximation the atomic potential (including the nucleus) may be written as:

$$\begin{aligned} V_a(x,y,z) &= 2\pi^2 a_0 e \sum_{i=1}^{3} \frac{a_i}{r} \exp(-2\pi r\sqrt{b_i}) + \\ & 2\pi^{5/2} a_0 e \sum_{i=1}^{3} c_i d_i^{-3/2} \exp(-\pi^2 r^2/d_i) \\ & \text{with} \quad r^2 = x^2 + y^2 + z^2, \end{aligned} \tag{5.9}$$

where a_0 is the Bohr radius and the a_i, b_i, c_i, and d_i coefficients are tabulated in Appendix C. There is a different set of coefficients for each element. A graph of the atomic potential vs. radius in three dimensions is shown in Fig. 5.4 for a few selected elements.

When the atomic potential is integrated along the z direction (i.e., the optic axis of the microscope) the result is the projected atomic potential:

$$\begin{aligned} v_z(x,y) &= \int_{-\infty}^{+\infty} V_a(x,y,z)\mathrm{d}z \\ &= 4\pi^2 a_0 e \sum_{i=1}^{3} a_i K_0(2\pi r\sqrt{b_i}) + 2\pi^2 a_0 e \sum_{i=1}^{3} \frac{c_i}{d_i} \exp(-\pi^2 r^2/d_i) \\ & \text{with} \quad r^2 = x^2 + y^2, \end{aligned} \tag{5.10}$$

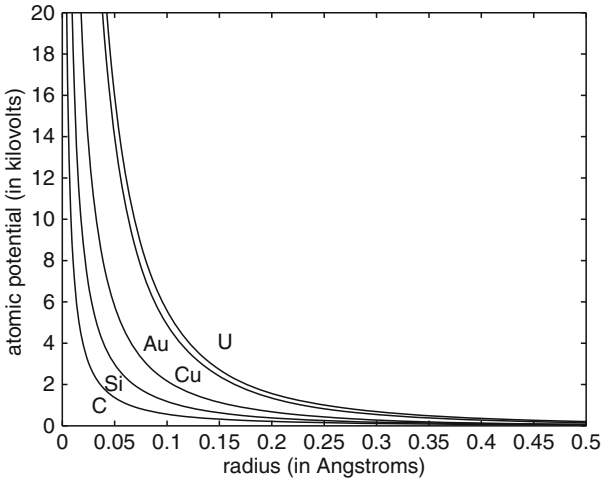

Fig. 5.4 Calculated atomic potential vs. the three dimensional radius r for isolated single atoms at $r = 0$. The atoms are carbon (Z = 6), silicon (Z = 14), copper (Z = 29), gold (Z = 79), and uranium (Z = 92)

where $K_0(x)$ is the modified Bessel function of zeroth order. The projected atomic potential is shown in Fig. 5.5 for the same elements as in Fig. 5.4.

The atomic nucleus is essentially a point charge on this scale (typical nuclear sizes are of order a few times 10^{-5}Å). This causes a singularity in the projected

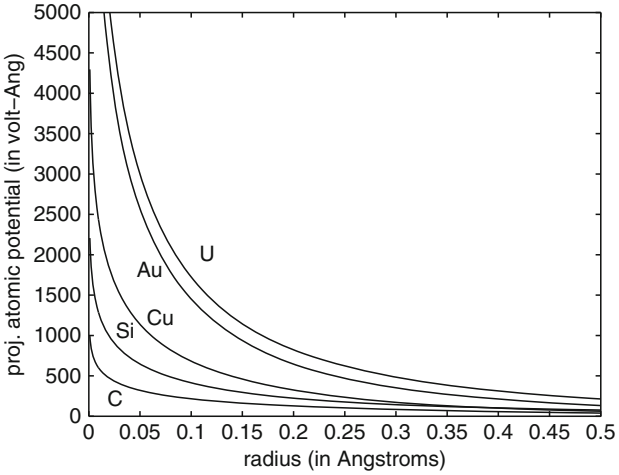

Fig. 5.5 Calculated projected atomic potential vs. the two dimensional radius r for isolated single atoms at r = 0. The atoms are carbon (Z = 6), silicon (Z = 14), copper (Z = 29), gold (Z = 79), and uranium (Z = 92)

atomic potential at $r = 0$ (there is also a singularity in the 3D atomic potential.) In reality the finite size of the nucleus removes the singularity so there is no real problem. No electron microscope that currently exists has enough resolution to see this strong singularity either, so the limited resolution of the microscope will further smear out this singularity in practice. In practical computer simulations the singularity will also be removed by finite sampling requirements because only the projected atomic potential averaged over a nonzero sized sampling element or pixel is used. The projected atomic potential (Fig. 5.5) diverges less strongly than the atomic potential (Fig. 5.4).

At a radius of 0.1Å the projected atomic potential of silicon (Si) is 0.41 kV-Å and the projected atomic potential of gold (Au) is 1.45 kV-Å (see Fig. 5.5). The interaction parameter σ (5.6) is 0.92 radians/(kV-Å) at a beam energy of 100 keV. This means that a single silicon atom will produce a total phase shift of 0.38 radians and a single gold atom will produce a phase shift of 1.34 radians (both at a beam energy of 100 keV and a radius of 0.1 Å). A single gold atom is not a weak phase object [in the sense of (3.6)] but a single silicon atom is a reasonable weak phase object (at 100 keV). The situation improves slightly at beam energies of 300 keV or above because σ decreases by almost a factor of two. All atoms have a near singularity at a radius of zero so no single atom is truly a weak phase object in a strict sense.

5.2.3 Atomic Size

There is no single unambiguous method to calculate the effective size of single atoms. The rms (root-mean-square) radius is as good as any other method. The three dimensional mean square (rms) radius of the charge distribution can be defined as:

$$r_q = \left[\frac{\int_0^\infty r^2 \rho(r) r^2 \mathrm{d}r}{\int_0^\infty \rho(r) r^2 \mathrm{d}r} \right]^{1/2} \quad \text{where} \quad r = x^2 + y^2 + z^2, \tag{5.11}$$

where $\rho(r)$ is the radial charge density. In a similar manner the two dimensional mean square radius of the projected atomic potential is:

$$r_v = \left[\frac{\int_0^\infty r^2 v_z(r) r \mathrm{d}r}{\int_0^\infty v_z(r) r \mathrm{d}r} \right]^{1/2} \quad \text{where} \quad r = x^2 + y^2. \tag{5.12}$$

Portions of the potential at large radius contribute more to this calculation due to their increased effective area. For example if the projected atomic potential is multiplied by r the result is shown in Fig. 5.6. The rms atomic radii for all atoms as calculated from (5.11) and (5.12) is shown in Fig. 5.7. The large tails of the potential increase the apparent size of the atoms. The effective rms size of the atoms as

determined by the projected atomic potential is about two Angstroms in diameter. Note that the effective full-width-half-maximum of a single atom image may be smaller because of the strong potential near the nucleus of each atom.

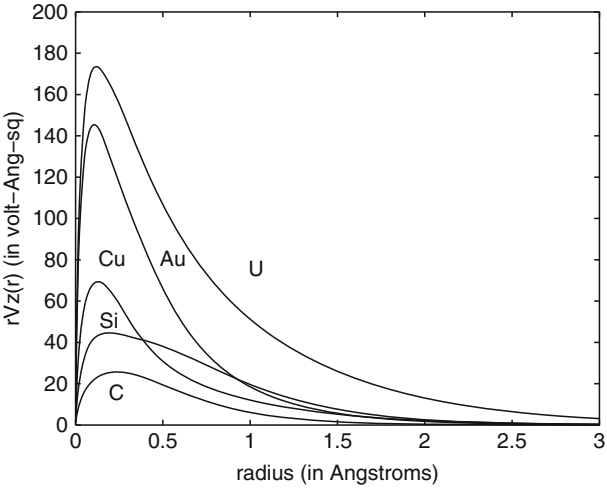

Fig. 5.6 Projected atomic potential multiplied by the radius r to illustrate the relative contribution to an image. Each curve is a different atom; carbon (Z = 6), silicon (Z = 14), copper (Z = 29), gold (Z = 79), and uranium (Z = 92)

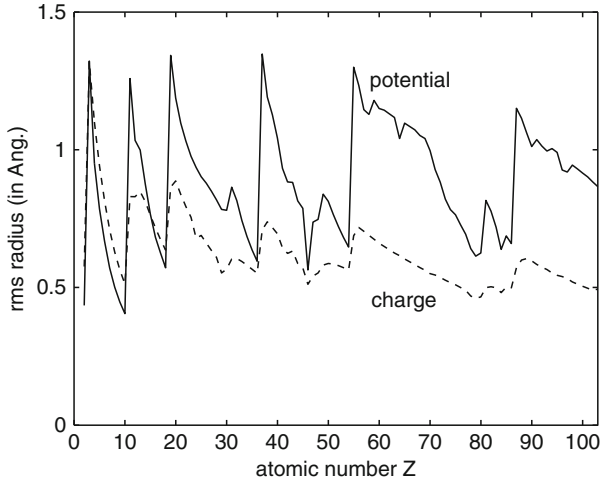

Fig. 5.7 The rms radius of isolated single atoms as determined from the (3D) electron charge and the (2D) projected atomic potential

5.2.4 Scattering Factors

The traditional physics view of electron scattering starts with a plane wave incident on the atom which gives rise to an outgoing plane wave plus an outgoing spherical wave (the atom has spherical symmetry) with amplitude $f_e(q)$.

$$\psi(\mathbf{x}) = \exp(2\pi \mathrm{i} k_z z) \quad \text{incident} \tag{5.13}$$

$$= \exp(2\pi \mathrm{i} k_z z) + f_e(q)\frac{\exp(2\pi \mathrm{i}\mathbf{q}\cdot\mathbf{r})}{r} \quad \text{scattered}, \tag{5.14}$$

where $\mathbf{q}$ is the difference between the incident and scattered wave vectors (three dimensional vector). The scattering amplitude $f_e(q)$ can also be referred to as the scattering factor. There are several methods of calculating the scattering amplitudes. The most popular approximation to the scattering amplitude is the first Born approximation that is simply the three dimensional Fourier transform of the atomic potential (see for example Sect. 38 of Schiff [312]):

$$f_e(\mathbf{q}) = \frac{2\pi m_0 e}{h^2}\int V_a(\mathbf{r})\exp(2\pi \mathrm{i}\mathbf{q}\cdot\mathbf{r})\mathrm{d}^3 r$$

$$= \frac{1}{2\pi e a_0}\int V_a(\mathbf{r})\exp(2\pi \mathrm{i}\mathbf{q}\cdot\mathbf{r})\mathrm{d}^3 r, \tag{5.15}$$

where $V_a(\mathbf{r})$ is the 3D atomic potential of the atom, m_0 is the rest mass of the electron, e is the magnitude of the charge of the electron, h is Planck's constant, and $a_0 = \hbar^2/m_0 e^2 = 0.5292\text{Å}$ is the Bohr radius. $f_e(q)$ is in units of Å and must be multiplied by the relativistic mass ratio m/m_0 for different incident electron energies. For the case where the atom is spherically symmetric this reduces to:

$$f_e(q) = \frac{1}{\pi e a_0 q}\int_0^\infty V_a(r)\sin(2\pi q r) r \mathrm{d}r. \tag{5.16}$$

The scattering factor is the amplitude for scattering of a single electron by a single atom. The first Born approximation is totally inadequate for directly calculating electron scattering in the electron microscope image (Zeitler and Olsen [388, 389], Glauber and Shoemaker [121]). In general $f_e(q)$ should be a complex valued quantity but the first Born approximation only yields a real valued quantity. However the first Born approximation is convenient because it is also the Fourier transform of the atomic potential. Image simulation will eventually use the specimen potential directly and not the scattering factors, so the Born approximation is still useful as a means of calculating the specimen potential. Combined with the Fourier projection theorem (Appendix B) the Born approximation provides a convenient method of calculating the projected atomic potential of thin specimens. It is also independent of the incident electron energy so that is easy to tabulate. As given in Appendix C the scattering amplitude in the first Born approximation can be written as:

$$f_e(q) = \sum_{i=1}^{3} \frac{a_i}{q^2 + b_i} + \sum_{i=1}^{3} c_i \exp(-d_i q^2), \tag{5.17}$$

where the a_i, b_i, c_i, and d_i coefficients are tabulated in Appendix C for each element and are found by fitting the results of the relativistic Hartree-Fock program. The scattering factors for several atoms are plotted in Fig. 5.8. Note that the scattering factor for carbon (Z = 6) and silicon (Z = 14) cross at low angle. The low angle scattering factor is dependent on the state of the outer valence shell which fills periodically with increasing atomic number in the periodic chart. The scattering factor at large angles is primarily due to the scattering from the nucleus which is a monotonic function of atomic number Z. Doyle and Turner [82] have given the most popular tabulation currently in use. Many other authors have tabulated relevant parameters for single atoms and Table C.1 of appendix C gives a more complete listing of the data available in the literature.

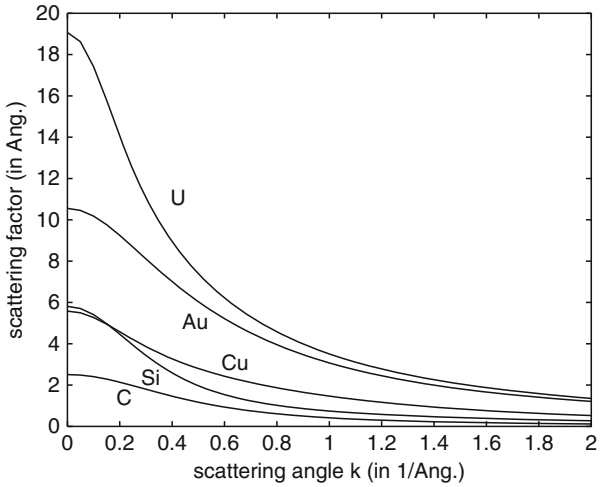

Fig. 5.8 The electron scattering factor in the first Born approximation vs. scattering angle $k = \alpha/\lambda$ of isolated single atoms. Each curve is a different atom which are carbon (Z = 6), silicon (Z = 14), copper (Z = 29), gold (Z = 79), and uranium (Z = 92)

A more detailed derivation of the scattering factor in the Moliere [252] or eikonal [312] approximation yields an improved expression of:

$$f_e(q) = \frac{2\pi \mathrm{i}}{\lambda} \int_0^\infty J_0(2\pi q r) \left\{ 1 - \exp\left[i\sigma \int V(x,y,z) \mathrm{d}z \right] \right\} r \mathrm{d}r \tag{5.18}$$

where $r = \sqrt{x^2 + y^2}$ can also be interpreted as the impact parameter, $J_0(x)$ is the Bessel function of order zero which arises from the azimuthal integration of a spherically symmetric function and σ is the interaction parameter (5.6). This expression for the electron scattering factor (5.18) is a complex quantity (Zeitler and Olsen

[388, 389], Frank [110], Reimer and Gilde [297], Ferwerda and Visser [103]) and can be recognized as the Fourier transform of the weak phase object approximation (5.5). The scattering processes discussed here are purely elastic so electrons should not be created or destroyed. The optical theorem (for example Schiff [312]) requires that the scattering factor $f_e(q)$ be complex to preserve the total number of electrons. A complex valued scattering factor does not imply that the atomic potential is complex. The atomic potential is a real valued function but a complete elastic scattering factor should be complex to preserve the total number of particles. The Moliere approximation for $f_e(q)$ (5.18) is a different value for each incident electron energy and is therefore difficult to tabulate for a general incident electron energy. The first Born approximation can be tabulated independent of energy which probably accounts for its popularity. The scattering amplitude is plotted in Fig. 5.9 in both the Moliere and Born approximations. The first Born approximation gets the magnitude about right but gets the phase of the scattering amplitude completely wrong. The phase of $f_e(q)$ increases dramatically at high angles whereas the phase of the first Born approximation is identically zero for all angles.

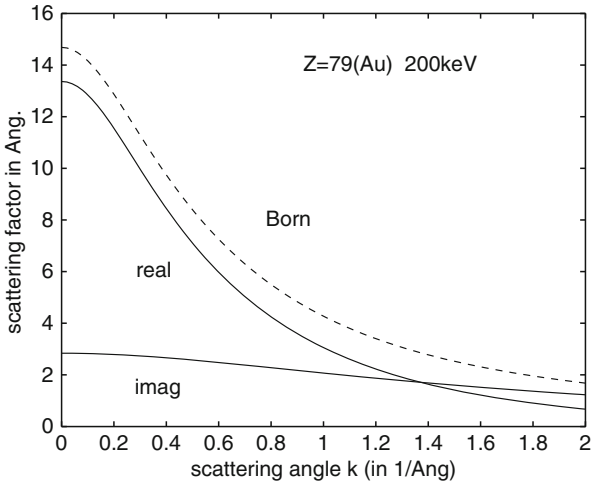

Fig. 5.9 The electron scattering factor for gold at 200 keV. The curves labeled real and imag. are the complex scattering factor in the Moliere approximation (5.18) and the curve labeled Born is the scattering factor in the first Born approximation scaled by the relativistic mass ratio m/m_0

5.3 Total Specimen Potential

The imaging electrons in the microscope interact with the effective potential of the specimen as a whole. Simulation of a whole electron microscope image requires a knowledge of the position of all atoms in the specimen. The main question is how to

combine the single atom potentials to get the potential of the whole specimen. The simplest approach is to form the potential of the specimen by a linear superposition of the potentials of each atom in the specimen.

$$v_z(\mathbf{x}) = \sum_{j=1}^{N} v_{zj}(\mathbf{x} - \mathbf{x}_j) \tag{5.19}$$

where $\mathbf{x}_j = (x_j, y_j)$ is the position of atom j in a plane perpendicular to the optical axis of the microscope and $v_{zj}(\mathbf{x})$ is its projected atomic potential. This linear superposition approximation would be exact for single atoms separated by a distance that is large compared to the size of the atom. However, in an actual solid specimen the atoms are bound together and their outer valence electrons will have been rearranged slightly. This electronic rearrangement will also alter the projected atomic potential (and low angle scattering) slightly. The principle interaction causing high angle scattering is the interaction between the imaging electrons (in the microscope) and the large point charge at the atomic nucleus. Because the nucleus is unaffected by bonding in the solid the high angle scattering (as in ADF-STEM) should be well represented by a simple linear superposition of atomic potentials. The bonding in the solid should primarily affect the low angle scattering such as in bright field phase contrast (STEM and CTEM).

Inherent in the discussion of Sect. 5.2 is the assumption that each atom is spherically symmetric. This is only true for atoms whose valence shells are in the $l = 0$ or s angular momentum state. Early work by McWeeny [238, 239] and Freeman [112, 113] showed that the X-ray scattering from aspherical atoms (p-state valence shells) may vary by approximately 5%–10% with azimuthal angle in low Z atoms at small scattering angles. Electronic rearrangement in the solid should produce a similar magnitude of error in the projected atomic potential of the specimen. The error introduced with the linear superposition of atomic potentials approximation should be regarded as about 5% to 10% in the low angle scattering. This is an acceptable error for many calculations but caution should be taken when trying to extract precise quantitative information out of a simulation.

It is straight forward to write a general purpose computer program to calculate images of thin specimens with any element in the periodic chart that runs in a reasonable amount of computer time using the linear superposition of tabulated single atom potentials from appendix C (or other similar tabulations). Unfortunately, computing the electronic structure of solids including bonding is still a demanding task. It is not yet easy to write a general purpose computer program to calculate the electronic structure of an arbitrary solid, both because the theory is still under development to some extent and because of the large amount of computer time required. With the rapid advances in computational science this situation will likely improve in the near future, but for now a simple linear superposition (5.19) will have to suffice.

Previous tabulations of single atom properties usually were stated in terms of the electron scattering factors in the first Born approximation (5.15). The first Born approximation is totally inadequate to describe the scattering process but has a

simple relationship to the atomic potential (as well as the X-ray scattering factors, see appendix C). The scattering factors in the first Born approximation naturally lend themselves to a calculation of the projected atomic potential in reciprocal (or Fourier) space. Once the potential has been calculated then a more correct scattering factor (5.18) or specimen transmission function can be calculated (5.7) from the specimen potential. The Fourier transform of (5.19) is:

$$V_z(\mathbf{k}) = \sum_{j=1}^{N} V_{zj}(\mathbf{k}) \exp(2\pi \mathrm{i}\mathbf{k} \cdot \mathbf{x}_j) \tag{5.20}$$

substituting the electron scattering factor in the first Born approximation yields:

$$\sigma V_z(\mathbf{k}) = \lambda \frac{m}{m_0} \frac{1}{ab} \sum_j f_{ej}(k_x, k_y, 0) \exp(2\pi \mathrm{i}\mathbf{k} \cdot \mathbf{x}_j), \tag{5.21}$$

where $f_{ej}(\mathbf{q})$ is the electron scattering factor in the first Born approximation for atom j. The total area of the specimen being simulated (with supercell dimensions $a \times b$) is ab and is required to normalize the Fourier transform properly. This constant may vary with different implementations of the Fourier transform. Note that $f_{ej}(\mathbf{q})$ is a function of a three dimensional wave vector $\mathbf{q} = (k_x, k_y, k_z)$ but the inverse transform is with respect to only two dimensions ($\mathbf{k} = (k_x, k_y)$) with zero for the third coordinate k_z. This results in the projected atomic potential (i.e., integration along the z axis) because of the Fourier projection theorem (see appendix B). The real space atomic potential can be found by inverse Fourier transforming $V_z(\mathbf{k})$ as:

$$v_z(\mathbf{x}) = \mathrm{FT}^{-1}[V_z(\mathbf{k})]. \tag{5.22}$$

This $v_z(\mathbf{x})$ can be used in (5.18) or (5.7). The summation on the right hand side of (5.21) is formally called the structure factor of the specimen given by:

$$F(\mathbf{q}) = \sum_j f_{ej}(\mathbf{q}) \exp(2\pi i \mathbf{q} \cdot \mathbf{x}_j). \tag{5.23}$$

If the specimen is a crystal then there will be a few discrete points $\mathbf{k}$ at which the Fourier component of the potential $V_z(\mathbf{k})$ is significantly larger than its neighboring values. These correspond to the Bragg reflections for this particular projection of the crystal. The Fourier components of the potential are zero at points in between the Bragg reflections for crystalline specimens. Thermal vibration of the atoms in the specimen may cause a small diffuse background in between the Bragg peaks (thermal diffuse scattering, TDS). If the specimen is amorphous then there will be a nearly continuous distribution of values at all points $\mathbf{k}$ in reciprocal space. Crystals containing defects or interfaces should be treated as if they are amorphous and all Fourier components of the potential should be calculated (i.e., not just the Bragg reflections).

5.4 BF Phase Contrast Image Calculation

This section will be discussed in the context of BF-CTEM image formation although it also applies to BF-STEM via the reciprocity theorem. In simple coherent BF-CTEM image formation the electron wave function incident on the specimen is a single plane wave of unit intensity. This wave function will pass through a thin specimen and experience a position dependent phase shift modeled as the specimen transmission function. Once the projected atomic potential of the specimen has been calculated (5.19 and 5.21) it is relatively straight forward to calculate the actual electron microscope image. From the projected atomic potential the wave function transmitted through the specimen is:

$$\psi_t(\mathbf{x}) = t(\mathbf{x})\exp(2\pi i k_z z) \sim t(\mathbf{x}), \tag{5.24}$$

where a common factor of $\exp(2\pi i k_z z)$ has been ignored (it will drop out because only the intensity matters in the end and it is unaffected by the transfer function). The specimen transmission function is:

$$t(\mathbf{x}) = \exp\left[i\sigma v_z(\mathbf{x})\right], \tag{5.25}$$

where $v_z(\mathbf{x})$ is the total projected atomic potential of the specimen (5.8, 5.22) and σ is the interaction parameter (5.6).

The electron microscope image is fundamentally cylindrically symmetric. It is essential that any simulation preserve this symmetry. Figure 5.10 shows a view of a sampled image in reciprocal space. The real space dimensions are $a \times b$ (in x and y). The general case in which a and b are very different is shown. There are two things that may alter the basic symmetry of the image and produce odd artifacts in the image. First, if the real space image size is not the same in x and y then the maximum spatial frequency may be different in each direction. The second related problem is the few Fourier coefficient in the four corners. If the entire area of the Fourier transform is just filled completely then various artifacts with rectangular symmetry can creep into the image. It is usually advisable to bandwidth limit the image with cylindrical symmetry. Only the spatially frequencies inside the largest inscribed circle as shown in (5.10) should be allowed to contribute to the final image. Although this may limit the resolution a little it at least does it with the proper symmetry and introduces fewer nonphysical artifacts in the image. This also means that it is best to make the image size square, otherwise a large percentage of the pixels will have to be set to zero and the calculation will not be very efficient. This bandwidth limit should be applied to both the projected atomic potential and the transmission function because the calculation in (5.25) is nonlinear and will generate many higher frequencies even though $v_z(\mathbf{x})$ may be properly bandwidth limited.

The transmitted wave function (5.24) is imaged by the objective lens of the microscope. The effects of the aberrations of the objective lens are easiest

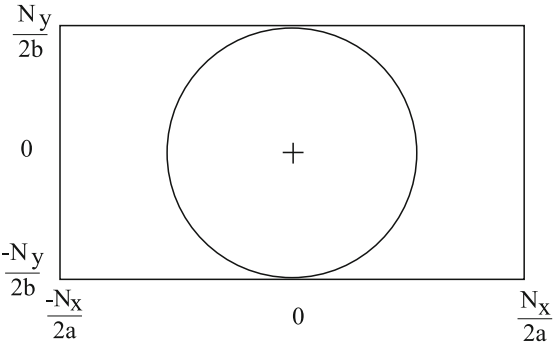

Fig. 5.10 Symmetrical bandwidth limiting the image in reciprocal space. The real space image has dimensions of $a \times b$ (in x and y) and is sampled with $N_x \times N_y$ pixels. Only those Fourier components inside the *largest inscribed circle* should be allowed to contribute to the image to avoid artifacts with an incorrect symmetry

to calculate by Fourier transforming the transmitted wave function and then multiplying by the transfer function of the objective lens.

$$\begin{aligned} \Psi_t(k) &= \mathrm{FT}[\psi_t(\mathbf{x})] \\ \Psi_i(k) &= \Psi_t(\mathbf{k}) H_0(\mathbf{k}), \end{aligned} \tag{5.26}$$

where $\Psi_i(k)$ is the image wave function in the back focal plane of the objective lens and $H_0(k)$ is the transfer function of the objective lens.

$$\begin{aligned} H_0(\mathbf{k}) &= \exp[-\mathrm{i}\chi(\mathbf{k})] A(\mathbf{k}) \\ \chi(k) &= \pi\lambda k^2 (0.5 C_s \lambda^2 k^2 - \Delta f), \end{aligned} \tag{5.27}$$

where Δf is defocus, C_s is the coefficient of spherical aberration and $A(\mathbf{k})$ is the aperture function:

$$\begin{aligned} A(\mathbf{k}) &= 1; \quad \lambda k = \alpha < \alpha_{\max} \\ &= 0; \quad \text{otherwise} \end{aligned} \tag{5.28}$$

$\alpha_{\max}$ is the maximum semiangle allowed by the objective aperture. Other aberrations may be included but only the simplest few are given here for simplicity. The objective lens images this wave function to form the final electron microscope image. The actual magnification of the objective lens may be ignored in the calculation (but NOT in practice) if the image coordinates are always referred to the actual specimen dimensions.

The actual recorded image $g(\mathbf{x})$ is the magnitude squared of the image wave function after inverse Fourier transforming back into real space.

$$\begin{aligned} \psi_i(\mathbf{x}) &= \mathrm{FT}^{-1}[\Psi_i(\mathbf{k})] \\ g(\mathbf{x}) &= |\psi_i(\mathbf{x})|^2 = |\psi_t(\mathbf{x}) \otimes h_0(\mathbf{x})|^2, \end{aligned} \tag{5.29}$$

where $h_0(\mathbf{x})$ is the complex point spread function of the objective lens (the inverse Fourier transform of $H_0(\mathbf{k})$). The steps required to calculate the image of a thin specimen are summarized in algorithmic form in Table 5.1.

Table 5.1 Steps in the simulation of CTEM images of thin specimens (a phase grating calculation)

Step 1	Calculate the projected atomic potential $v_z(\mathbf{x})$ from (5.19) or (5.21).
Step 2	Calculate the transmission function $t(\mathbf{x}) = \exp[i\sigma v_z(\mathbf{x})]$ (5.25) and symmetrically bandwidth limit it. The incident wave function is a plane wave so the transmitted wave function is equal to the transmission function.
Step 3	Fourier transform the transmission function $T(\mathbf{k}) = \mathrm{FT}[t(\mathbf{x})]$.
Step 4	Multiply the Fourier transform of the transmission function by the transfer function of the objective lens, $H_0(k)$ (5.27) to get the image wave function in the back focal plane $\Psi_i(\mathbf{k}) = H_0(k)T(\mathbf{k})$.
Step 5	Inverse Fourier transform the image wave function $\psi_i(\mathbf{k}) = \mathrm{FT}^{-1}[\Psi_i(\mathbf{k})]$.
Step 6	Calculate the square modulus of the image wave function (in real space) to get the final image intensity $g(\mathbf{x}) = \lvert\psi_i(\mathbf{x}) \otimes h_o(\mathbf{x})\rvert^2$.

5.4.1 Single Atom Images

Figure 5.11 shows the specimen transmission function (5.25) for the five single atoms plotted in Fig. 5.5. The atoms are arranged in a row 10 Å apart. The atomic potential was calculated in an image size of 50 Å on a side and 512×512 pixels using (5.21). The slight ringing near each atom is due to the finite bandwidth of the sampled image. There is also a slight asymmetry in some of the atoms. This occurs because there will always be some atom positions that are not exactly integer multiples of the pixel spacing. The atom potential is then spread across neighboring pixels in a nonsymmetrical manner. This asymmetry should be small and vanish in the final images. Also note that the real part of the transmission function has a stronger dependence on atomic number Z than the imaginary part.

The actual height of the peak for each atom is mainly a function of the sampling size. The actual potential has a singularity at the center of each atom (see Fig. 5.5). The value at the center of the atom is the average over one pixel. As this pixel gets smaller this value is closer to the singular value at the center of the atom. The integrated value should come through to the image properly with different pixel sizes although some care is required in choosing an appropriate pixel sampling size.

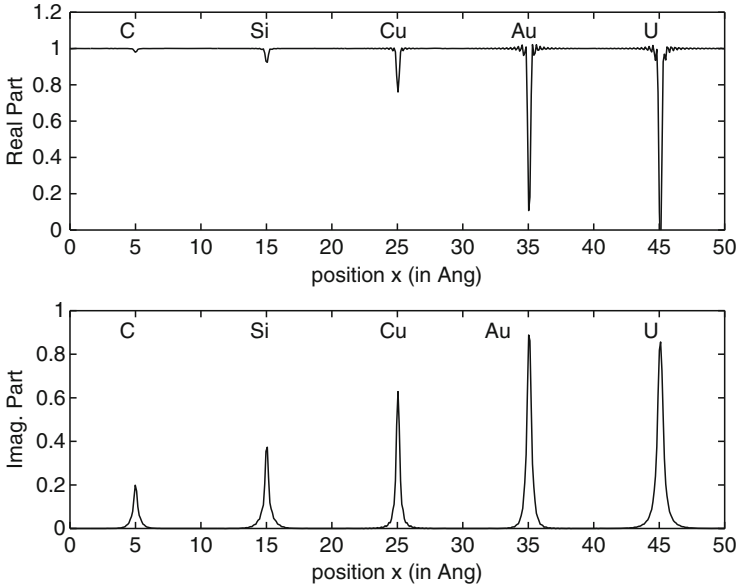

Fig. 5.11 Line scan of the complex transmission function for five isolated single atoms and an incident electron beam energy of 200 keV. This was calculated with a sampled image of 512×512 pixels. The scan goes through the center of each atom (atomic number Z = 6,14,29,79,92)

Figure 5.12 shows the image intensity (5.29) of the five isolated single atoms calculated from Fig. 5.11 with Scherzer conditions. The incident electron intensity is assumed to be unity for this simulation so that the image intensity in between the atoms (i.e., vacuum) should be one. The rings surrounding each atom are part of the so-called Airy disk caused by a sharp cut off in reciprocal space due to the objective aperture. The rings on the right wrap around to interfere with the atom on the left (the wrap-around effect). Figure 5.13 show a line scan through the center of each atom in Fig. 5.12. Eisenhandler and Siegel [89] and Reimer and Gilde [297] have also plotted single atom image profiles.

In the special case of isolated single atoms the image intensity $g(\mathbf{x})$ in bright field phase contrast may be written as:

$$g(\mathbf{x}) = \left| 1 + 2\pi \mathrm{i} \int_0^{k_{\max}} f_e(k) \exp[-\mathrm{i}\chi(k)] J_0(2\pi k r) k \mathrm{d}k \right|^2 \tag{5.30}$$

where $f_e(k)$ is the electron scattering factor in the Moliere approximation (found by numerical integration of (5.18) using the projected atomic potential from appendix C), $\chi(k)$ is the aberration function, $k_{\max} = \alpha_{\max}/\lambda$ is the maximum spatial frequency in the objective aperture and $J_0(x)$ is the Bessel function of order zero. Note that the first Born approximation for the scattering factor should not be used in this expression. A graph of the peak single atom signal $1 - g(0)$ in coherent bright

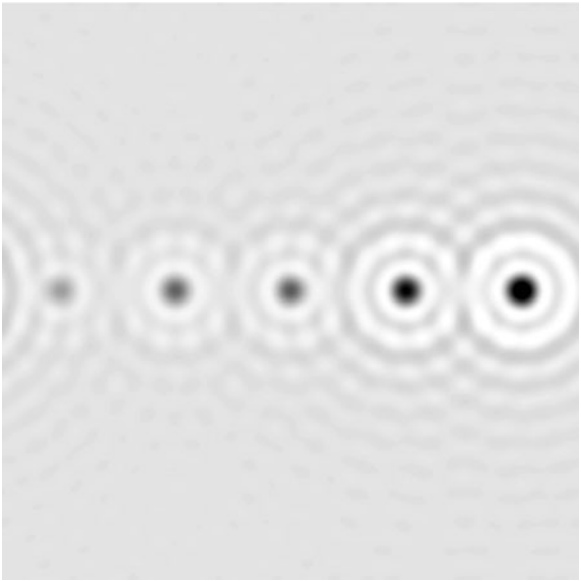

Fig. 5.12 The coherent bright field phase contrast image of five isolated single atoms and an incident electron beam energy of 200 keV. The electron optical parameters are spherical aberration $C_s = 1.3$ mm, defocus $\Delta f = 700$ Å and an objective aperture of 10.37 mrad (Scherzer conditions). This was calculated with a sampled image of 512×512 pixels. Atomic number Z = 6(C),14(Si),29(Cu),79(Au),92(U) (left to right). The image ranges from 0.72 (*black*) to 1.03 (*white*)

field phase contrast found by numerical integration of (5.30) is shown in Fig. 5.14. The BF signal varies weakly with atomic number. The overall trend approximately follows $Z^{0.6}$ to $Z^{0.7}$ however there is a significant variation reflecting the filling of different valence shells as in the periodic chart. Note that different atomic numbers can have the same signal and heavier atoms can have a smaller signal than lighter atoms (the signal is not monotonic in atomic number Z). It is possible to distinguish heavy atoms and light atoms but it would not be possible to precisely identify any specific atom by its bright field phase contrast signal alone.

5.4.2 Thin Specimen Images

Silicon is a reasonable starting point to begin discussing image simulation. It is a low enough atomic number that it is reasonable to approximate it as a weak phase object and it has a relatively simple structure. A precise simulation should still include thickness effects as covered in later chapters but for now the geometrical effects of specimen thickness will be ignored. Thickness can be included in some sense by

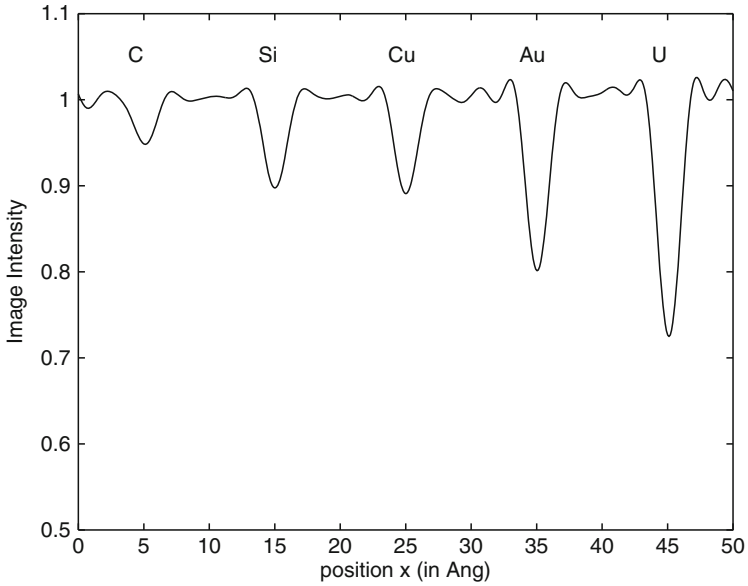

Fig. 5.13 Line scan through the center of the atoms in the coherent bright field phase contrast image in Fig. 5.12

superimposing the atoms along the optic axis in the specimen but the position of each atom along the beam direction will be ignored until later.

Silicon is a technologically important material and is the basic building block of most electronic devices. Its common crystalline form is the diamond structure (two interpenetrating face centered cubic or fcc lattices). When viewed in the electron microscope the three-dimensional lattice is projected into a two dimensional image. The three common projections of the diamond lattice with a cubic cell dimension of a are shown in Fig. 5.15. The (100) projection has a repeat length of a along the beam direction with one atom per repeat length. The (110) projection repeats every $a\sqrt{2}$ with two atoms per repeat length and two different types of atomic layers. The (111) projection repeats every $a\sqrt{3}$ with two atoms per site and three different layers.

To calculate an image of silicon in the weak phase object approximation requires sampling the atomic potential of silicon in a rectangular grid with the atoms placed at their respective positions in the grid. The discrete Fourier transform (DFT or FFT) requires that the sampled image obey periodic boundary conditions so the boundaries of the sampled image should match the natural periodicity of the actual specimen. This means that the sampling grid size should be an integer number of unit cells shown in Fig. 5.15 or equivalent. The full scale dimensions of the sampling grid will be labeled a, b in the horizontal and vertical directions, respectively. This nomenclature is drawn from crystallography and should not be confused with the real physical dimensions of the crystal (which are also frequently labeled a, b, c).

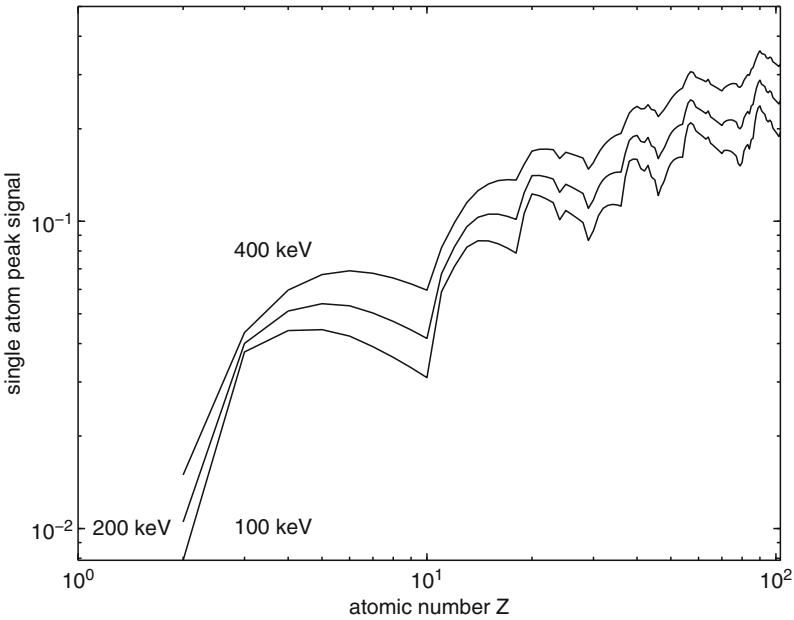

Fig. 5.14 Single atom peak signal in coherent bright field phase contrast vs. atomic number Z for incident electron energies of 100 keV, 200 keV, and 400 keV. Spherical aberration was fixed at $C_s = 1.3$ mm. Scherzer conditions were used for defocus and objective aperture

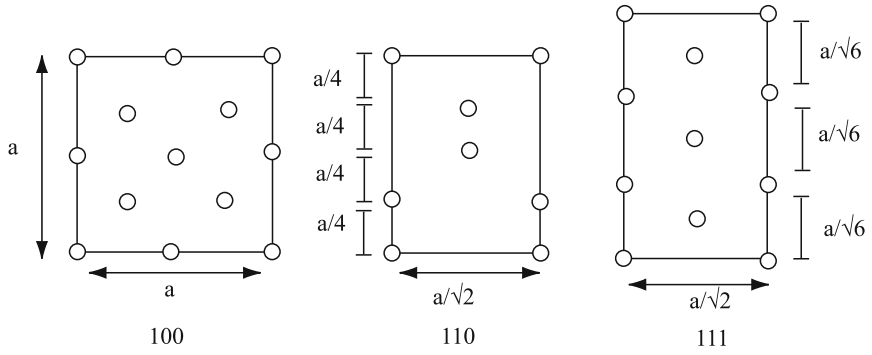

Fig. 5.15 Common projections of the silicon lattice (*diamond structure* with cubic cell size a = 5.43 Å). The *circles* represent the projected position of the silicon atoms. The indicated crystal direction (100, 110, or 111) is along the optic axis of the microscope and perpendicular to the plane of the paper

The meaning will usually be clear from the context in which they are used. As an example an image of the (110) projection of silicon will be calculated. The full scale dimensions of the (110) unit cell in Fig. 5.15 will be called $a_0 = a_{Si}/\sqrt{2}$ in the horizontal direction and $b_0 = a_{Si}$ in the vertical direction. a_{Si} is the the real physical cubic cell size of silicon.

It is tempting to make the real space sampling grid the same size as the two dimensional unit cell in Fig. 5.15 but this is not a good idea. A typical electron microscope has a resolution of no better than about 1.5–2Å. A good rule of thumb is to keep the real space sampling resolution $(\Delta x, \Delta y)$ to be no bigger than about 1/3–1/4 of the final resolution. This way atoms still look round and not rectangular. With $a_0 = 3.84$Å and $b_0 = 5.43$Å this would mean that $N_x = a_0/\Delta x \sim 7.7$ pixels and $N_y = b_0/\Delta y \sim 10.9$ pixels. Rounding up to the nearest power of two would give an image of 8 by 16 pixels. Although the real space sampling size is adequate the reciprocal space sampling is very wrong in this simple argument. There are actually two sampling requirements that must be meet. Both real space and reciprocal space are important. With a single unit cell of size $a_0 \times b_0$ the resolution in reciprocal space is $\Delta k_x = 1/a_0 = 0.26\text{Å}^{-1}$ and $\Delta k_y = 1/b_0 = 0.18\text{Å}^{-1}$. At 200 keV the electron wavelength is 0.02508Å. Using $\alpha = \lambda k$ means that this choice has an angular resolution of about 6.5 mrad and 4.6 mrad. In reciprocal space a typical objective aperture semiangle α is about 10 mrad. There would only be two or three pixels inside the objective aperture in the final image. This would be totally inadequate to sample the transfer function or the specimen. In practice it is a good idea to have at least 5–10 pixels in the radius of the objective aperture (much more is better).

The solution to this problem is slightly nonintuitive. The size of the sampled image should really be several times the size of the minimum unit cell of the crystal specimen. As long as a and b are integer multiples of a_0 and b_0 the periodic boundary conditions are satisfied, and the reciprocal space resolution can be improved (i.e., Δk_x and Δk_y made smaller). To get a reciprocal space sampling of about 1 mrad at 200 keV requires a supercell size of 7×5 unit cells (26.89×27.15 Å).

For this particular problem (a perfect crystal) expanding the number of unit cell in real space simply moves the Bragg peaks further apart in Fourier space with zero in between. The transfer function is not strictly needed at these in between zeros so there is no real improvement for this particular problem. However, in later examples with imperfect crystals and STEM probes this sampling will be important so this example will continue as if it were a more general problem, although there is some argument that this is not the most efficient approach (this is a quick calculation so CPU time is not much of a concern) for this particular problem.

The normalized coordinates for one projected unit cell of (110) silicon is shown in Table 5.2. The projected atomic potential for a four atom thick specimen of (110) silicon is shown in Fig. 5.16 a) with a super cell size of 7×5 silicon unit cells. Note the characteristic "dumb-bell" shape of pairs of silicon atoms. Figure 5.16 b,c) is the complex transmission function at a beam energy of 200 keV for this specimen and Fig. 5.17 a,b are the bright field images that would result at electron beam energies of 200 keV and 400 keV, respectively. The lattice is not easily visible at an energy of 100 keV under Scherzer conditions at this value of C_s. Deviations from Scherzer conditions can however produce some interesting effects (see for example Izui [180], Hutchison and Waddington [166]). When the image is calculated at 100 keV the result has a structure that resembles a crystal lattice but has a range that is of order 10^{-5} to 10^{-6} of its average value. This is just the roundoff error of the numerical calculation and has no physical significance. This can happen often

in simulation and you have to be careful to look at the actual numerical range of the image as well as its structure. The computer will just scale whatever numerical range is there to fill the available grey scale and produce an image. Although the dumb-bell shape is not resolved at either energy the higher voltage does start to get an elongated shape for the atom pairs. Spence et al. [333] and Desseaux et al. [78] have given a similar discussion of 110 germanium.

Table 5.2 The normalized coordinates for one projected unit cell of the silicon (Z=14) lattice in the (110) projection

Atom	Occupancy	x/a	y/b
1	1	0	0
2	1	0.5	0.75
3	1	0	0.25
4	1	0.5	0.5

The two dimensional unit cell dimensions are $a \times b$ where $a = a_{Si}/\sqrt{2} = 3.8396$Å and $b = a_{Si} = 5.43$Å

The apparent resolution of the simulated images in Fig. 5.17 is consistent with the linear image transfer function as shown in Fig. 5.18. The lowest order allowed reflection in the 110 projected unit cell (Fig. 5.15) are the 111 type beams with a spacing of $a_{Si}/\sqrt{3} = 3.13$Å, and the distance between the two atoms in the pair in the center of the unit cell is $a_{Si}/4 = 1.36$Å (Edington [87]). The larger of these spacing should be clearly resolved in all but the 100 keV case, but the smaller of these two should not be resolved at all, consistent with the simulation in Fig. 5.17.

5.4.3 Partial Coherence and the Transmission Cross Coefficient

The BF image intensity distribution is the square modulus of the transmitted wave function $\psi_t(\mathbf{x})$ convolved with point spread function $h_0(\mathbf{x})$ of the objective lens:

$$g(\mathbf{x}) = |\psi_t(\mathbf{x}) \otimes h_0(\mathbf{x})|^2 = [\psi_t(\mathbf{x}) \otimes h_o(\mathbf{x})]\,[\psi_t^*(\mathbf{x}) \otimes h_o^*(\mathbf{x})]\,. \tag{5.31}$$

The Fourier transform of this equation is:

$$\begin{aligned} G(\mathbf{k}) &= [\Psi_t(\mathbf{k})H_0(\mathbf{k})] \otimes [\Psi_t^*(-\mathbf{k})H_0^*(-\mathbf{k})] \\ &= \int \Psi_t(\mathbf{k}')H_0(\mathbf{k}')\Psi_t^*(\mathbf{k}'+\mathbf{k})H_0^*(\mathbf{k}'+\mathbf{k})\mathrm{d}^2\mathbf{k}' \\ &= \int T_{\mathrm{cc}}(\mathbf{k}',\mathbf{k}'+\mathbf{k})\Psi_t(\mathbf{k}')\Psi_t^*(\mathbf{k}'+\mathbf{k})\mathrm{d}^2\mathbf{k}', \end{aligned} \tag{5.32}$$

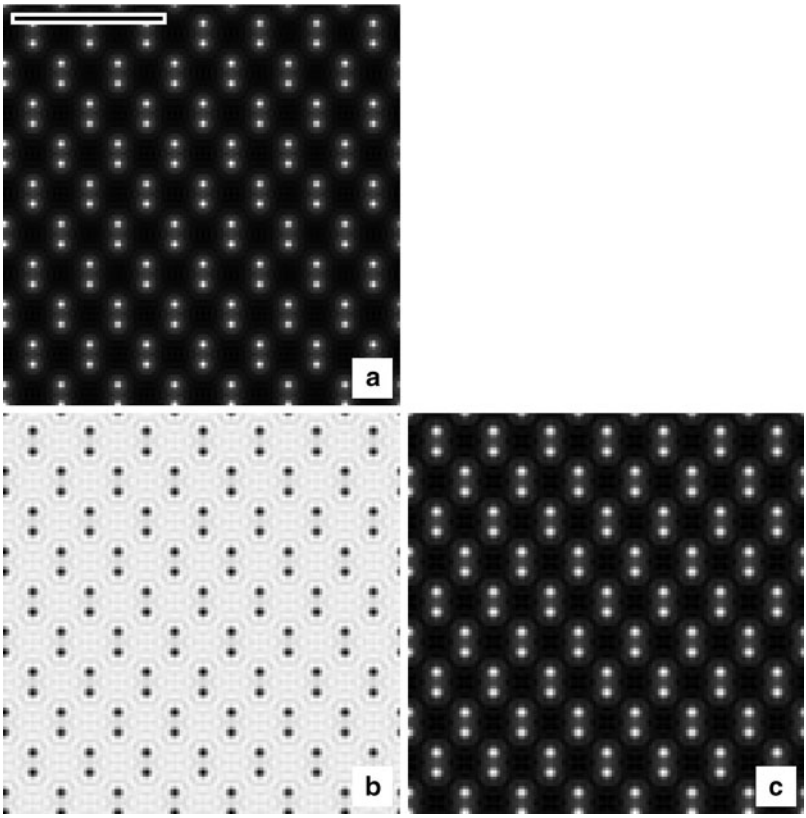

Fig. 5.16 Steps in simulating an image of 110 silicon in the weak phase object approximation. (a) Projected atomic potential (4 atoms thick, 128×128 pixels). (b,c) Real and imaginary part of the specimen transmission function at 200 keV. The scale bar in (a) is 10 Å. The image ranges are (b) 0.96–1.00, (c) 0.00–0.28. *White* is a larger positive number and atoms should appear white in (a)

where $T_{\mathrm{cc}}(\mathbf{k}', \mathbf{k}' + \mathbf{k})$ is the transmission cross coefficient that is similar to the function of the same name in light optics (for example Sect. 10.5.3 of Born and Wolf [34]). In the special case of perfectly coherent image formation the transmission cross coefficient (distinguished by an additional superscript coh) is:

$$T_{\mathrm{cc}}^{\mathrm{coh}}(\mathbf{k}', \mathbf{k}' + \mathbf{k}) = \exp\left[-\mathrm{i}\chi(\mathbf{k}') + \mathrm{i}\chi(\mathbf{k}' + \mathbf{k})\right] A(\mathbf{k}')A(\mathbf{k}' + \mathbf{k}), \tag{5.33}$$

where $\chi(\mathbf{k})$ is the aberration function of the objective lens (5.27) and $A(\mathbf{k})$ is the aperture function (5.28). The portion of the transmitted wave function that passes through the objective aperture is combined with itself as illustrated in Fig. 5.19. $\Psi_t(\mathbf{k})$ is duplicated and offset by a vector $\mathbf{k}$. The overlap region is multiplied by the transmission cross coefficient and the integrated value in the intersection of the two apertures forms a single Fourier component at position $\mathbf{k}$. The direct implementation (in a program) of the transmission cross coefficient for coherent imaging is rather inefficient. It would require the calculation of a two dimensional convolution

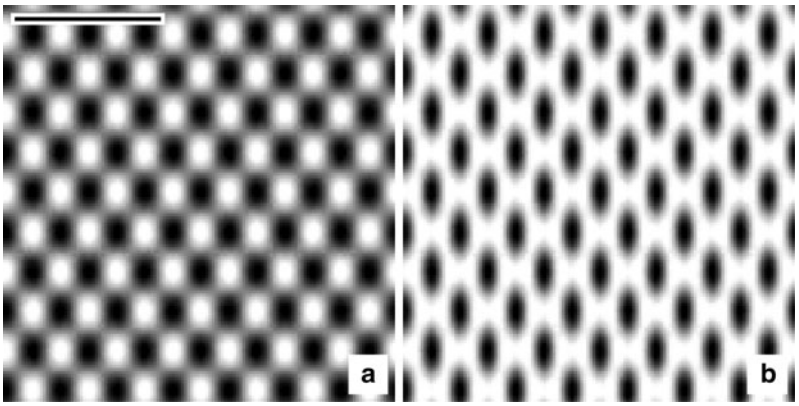

Fig. 5.17 Coherent bright field (BF) image of 110 silicon in the weak phase object approximation (128×128 pixels). (a) BF image at 200 keV, $\Delta f = 700$Å, $\alpha_{\max} = 10.37$ mrad. (b) BF image at 400 keV, $\Delta f = 566$Å, $\alpha_{\max} = 9.33$ mrad. Both have a spherical aberration of $C_s =$ 1.3 mm and Scherzer conditions. The scale bar in (a) is 10 Å. The image ranges are (a) 0.91–1.09, and (b) 0.87–1.07. White is a larger positive number and atoms should appear *black*

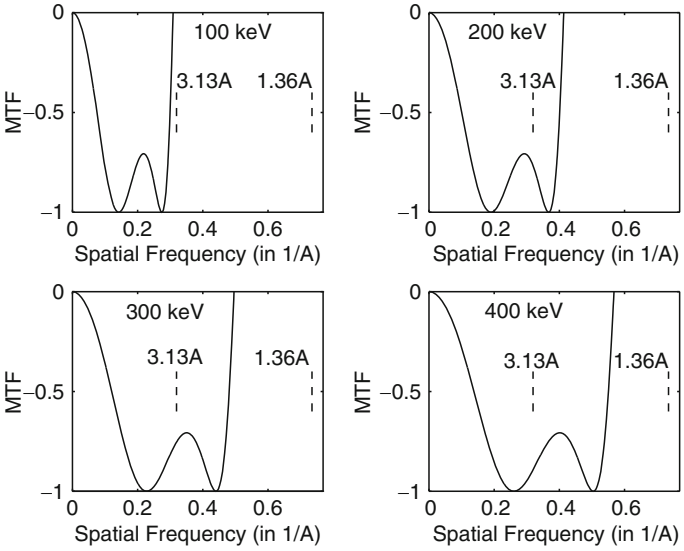

Fig. 5.18 The transfer function for a coherent bright field (BF) image in the weak phase approximation under Scherzer conditions. Spherical aberration is $C_s = 1.3$ mm and the electron energy varies from 100 kev to 400 keV. Two spacings relevant to the 110 projection of silicon are shown for comparison. About 1.36Å is the spacing between the dumbbells and 3.13Å is the spacing for the lowest order allowed reflection

at each point of reciprocal space (i.e., for each Fourier coefficient of the image). The use of the FFT as described earlier is much more efficient for coherent image formation.

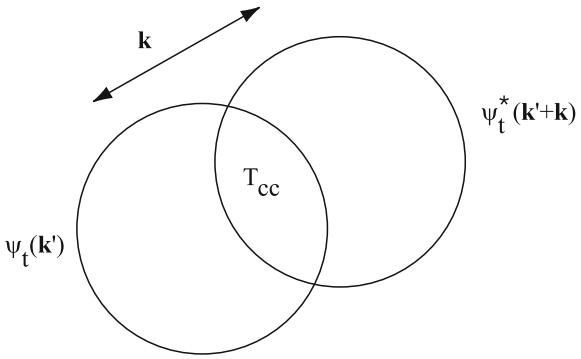

Fig. 5.19 The transmission cross coefficient in reciprocal space. Each *circle* represents the objective aperture. Only the overlap region labeled T_{cc} contributes to Fourier coefficient **k** in the image

The transmission cross coefficient however provides a mechanism for including the effects of partial coherence of strong phase objects as was discussed by O'Keefe [267], Ishizuka [173] and Pulvermacher [290]. (Bonevich and Marks [31] have also considered some higher order terms that are not discussed here.) If the specimen is thin enough to satisfy the weak phase object approximation then the form of the partial coherence derived in Sect. 3.2 is sufficient, however if the specimen contains heavy atoms or is many atoms thick then it may not be a weak phase object and a more detailed accounting of partial coherence is required. From the discussion on partial coherence in Sect. 3.2 the actual image will be formed with a small distribution of illumination angles and defocus values:

$$g(\mathbf{x}) = \int \left|\psi_t(\mathbf{x}) \otimes h_0(\mathbf{x}, \Delta f + \delta_f, \mathbf{k}_\beta)\right|^2 p(\mathbf{k}_\beta) p(\delta_f) \mathrm{d}\delta_f \mathrm{d}^2\mathbf{k}_\beta, \tag{5.34}$$

where δ_f is the deviation in defocus, $\mathbf{k}_\beta$ is the deviation in illumination angle and $p(\delta_f)$ and $p(\mathbf{k}_\beta)$ are their distributions. If the specimen is thin enough so that its geometrical extent along the optic axis can be ignored (as has been assumed in this chapter) then the illumination angle can be included in either the specimen or the transfer function of the objective lens. When included as part of the objective lens the integration over δ_f and $\mathbf{k}_\beta$ can be completely contained within the transmission cross coefficient without modifying the transmitted wave function $\psi_t(\mathbf{x})$. The transmission cross coefficient with partial coherence becomes:

$$\begin{aligned} &T_{cc}(\mathbf{k}', \mathbf{k}' + \mathbf{k}) = \\ &\int \exp\left[-i\chi(\mathbf{k}' + \mathbf{k}_\beta, \Delta f + \delta_f) + i\chi(\mathbf{k}' + \mathbf{k} + \mathbf{k}_\beta, \Delta f + \delta_f)\right] \\ &A(\mathbf{k}' + \mathbf{k}_\beta) A(\mathbf{k}' + \mathbf{k} + \mathbf{k}_\beta) p(\delta_f) p(\mathbf{k}_\beta) \mathrm{d}\delta_f \mathrm{d}^2\mathbf{k}_\beta. \end{aligned} \tag{5.35}$$

If the deviations from the coherent mode are assumed to be small then this expression can be Taylor expanded to first order in δ_{f} and $\mathbf{k}_\beta$ as:

$$\begin{aligned} &T_{\mathrm{cc}}(\mathbf{k}', \mathbf{k}'+\mathbf{k}) \\ &\quad = T_{\mathrm{cc}}^{\mathrm{coh}} \int \exp\{-\mathrm{i}[\mathbf{k}_\beta \cdot \frac{\partial}{\partial \mathbf{k}} + \delta_{\mathrm{f}} \frac{\partial}{\partial \Delta f} + \delta_{\mathrm{f}} \mathbf{k}_\beta \cdot \frac{\partial^2}{\partial \mathbf{k} \partial \Delta f} + \cdots] \\ &\qquad \left[\chi(\mathbf{k}') - \chi(\mathbf{k}'+\mathbf{k})\right]\} p(\delta_{\mathrm{f}}) p(\mathbf{k}_\beta) \mathrm{d}\delta_{\mathrm{f}} \mathrm{d}^2 \mathbf{k}_\beta, \end{aligned} \tag{5.36}$$

where the small variation of the aperture function with $\mathbf{k}_\beta$ has been ignored (or equivalently the aperture diameter is much larger than the maximum spatial frequency of interest in the image). The indicated derivatives are:

$$\begin{aligned} \mathbf{W}_{C1} &= \frac{\partial}{\partial \mathbf{k}} \left[\chi(\mathbf{k}') - \chi(\mathbf{k}'+\mathbf{k})\right] \\ &= 2\pi\lambda^3 C_s [|\mathbf{k}'|^2 \mathbf{k}' - |\mathbf{k}'+\mathbf{k}|^2 (\mathbf{k}'+\mathbf{k})] + 2\pi\lambda \Delta f \mathbf{k} \end{aligned} \tag{5.37}$$

$$\begin{aligned} W_{C2} &= \frac{\partial}{\partial \Delta f} \left[\chi(\mathbf{k}') - \chi(\mathbf{k}'+\mathbf{k})\right] \\ &= -\pi\lambda [|\mathbf{k}'|^2 - |\mathbf{k}'-\mathbf{k}|^2] \end{aligned} \tag{5.38}$$

$$\frac{\partial^2}{\partial \mathbf{k} \partial \Delta f} [\chi(\mathbf{k}') - \chi(\mathbf{k}'+\mathbf{k})] = 2\pi\lambda \mathbf{k}, \tag{5.39}$$

where the auxiliary symbols $\mathbf{W}_{C1}$ and W_{C2} will be used to simplify the derivation. Substituting for the derivatives yields:

$$\begin{aligned} &T_{\mathrm{cc}}(\mathbf{k}', \mathbf{k}'+\mathbf{k}) \\ &\quad = T_{\mathrm{cc}}^{\mathrm{coh}} \int \exp\{-\mathrm{i}\mathbf{k}_\beta \cdot \mathbf{W}_{C1} - \mathrm{i}\delta_{\mathrm{f}} W_{C2} - 2\pi\mathrm{i}\lambda \delta_{\mathrm{f}} \mathbf{k}_\beta \cdot \mathbf{k}\} \\ &\qquad p(\delta_{\mathrm{f}}) p(\mathbf{k}_\beta) \mathrm{d}\delta_{\mathrm{f}} \mathrm{d}^2 \mathbf{k}_\beta. \end{aligned} \tag{5.40}$$

Note that $\mathbf{W}_{C1}$ is a two dimensional vector quantity, as are all odd powers of $\mathbf{k}$. Assume that both the defocus and illumination angles have a Gaussian distribution:

$$p(\delta_{\mathrm{f}}) = \frac{1}{\Delta_0 \sqrt{\pi}} \exp(-\delta_{\mathrm{f}}^2 / \Delta_0^2) \tag{5.41}$$

$$p(\mathbf{k}_\beta) = \frac{1}{k_s^2 \pi} \exp(-\mathbf{k}_\beta^2 / k_s^2), \tag{5.42}$$

where δ_{f} and k_s are the $1/e$ widths of the two distributions. First perform the integration with respect to $\mathbf{k}_\beta$ giving:

$$\begin{aligned} &T_{\mathrm{cc}}(\mathbf{k}', \mathbf{k}'+\mathbf{k}) \\ &\quad = T_{\mathrm{cc}}^{\mathrm{coh}} \int \exp\left[-\mathrm{i}\delta_{\mathrm{f}} W_{C2} - k_s^2 |\mathbf{W}_{C1} + 2\pi\lambda \delta_{\mathrm{f}} \mathbf{k}|^2 / 4\right] p(\delta_{\mathrm{f}}) \mathrm{d}\delta_{\mathrm{f}}. \end{aligned} \tag{5.43}$$

Note that this is equivalent to Fourier transforming the distribution function $p(\mathbf{k}_\beta)$. Next perform the integration with respect to δ_f, and use $\beta = \lambda k_s$ (i.e., the condenser angle in radians) to give:

$$T_{cc}(\mathbf{k}', \mathbf{k}' + \mathbf{k}) = T_{cc}^{coh} \frac{1}{\sqrt{1 + \pi^2 \beta^2 \Delta_0^2 k^2}}$$
$$\times \exp\left[-\frac{\beta^2}{4\lambda^2} W_{C1}^2 + \frac{\Delta_0^2}{4} \frac{(\pi \beta^2 \mathbf{k} \cdot \mathbf{W}_{C1}/\lambda + i W_{C2})^2}{1 + \pi^2 \beta^2 \Delta_0^2 k^2} \right]. \tag{5.44}$$

The total transmission cross coefficient is a complicated damping factor whose net effect is similar to that for the weak phase approximation with linear imaging. However, the total transmission cross coefficient is much more complicated to calculate (note the vector nature of several components in the exponential factor). It is not separable into factors that depend only on $\mathbf{k}'$ and factors that depends only on $\mathbf{k}' + \mathbf{k}$. The image calculation with this form of partial coherence cannot be done using FFT's but must be done by an explicit weighted convolution in two dimensions (at each point in reciprocal space). This adds considerably to the required computer time but it is valid for a strongly scattering specimen with a negligible geometrical thickness such as several atomic layers of heavy atoms. If one of the deviations (defocus or angle) is small it may be more efficient to perform one integration analytically and the other numerically (possibly using FFTs) than to calculate the two dimensional convolution.

5.5 ADF STEM Images of Thin Specimens

In the STEM the objective lens acts on the electron beam before the beam interacts with the specimen in opposite order from the CTEM. The electrons that pass through the specimen and get scattered at high angles form the annular dark field or ADF signal. The wave function $\psi_p(\mathbf{x})$ of the focused probe incident upon the specimen at position $\mathbf{x}_p$ is formed by integrating the aberration wave function $\exp[-i\chi(\mathbf{k})]$ over the objective aperture as:

$$\psi_p(\mathbf{x}, \mathbf{x}_p) = A_p \int_0^{k_{max}} \exp[-i\chi(\mathbf{k}) - 2\pi i \mathbf{k} \cdot (\mathbf{x} - \mathbf{x}_p)] d^2\mathbf{k}, \tag{5.45}$$

where $\lambda k_{max} = \alpha_{max}$ is the maximum angle in the objective aperture and A_p is a normalization constant chosen to yield;

$$\int |\psi_p(\mathbf{x}, \mathbf{x}_p)|^2 d^2\mathbf{x} = 1. \tag{5.46}$$

In a practical sense the probe wave functions is easiest to calculate in Fourier space and then apply an inverse FFT.

$$\psi_p(\mathbf{x},\mathbf{x}_p) = A_p FT^{-1}\left\{\exp[-\mathrm{i}\chi(\mathbf{k}) + 2\pi\mathrm{i}\mathbf{k}\cdot\mathbf{x}_p]A(\mathbf{k})\right\}, \tag{5.47}$$

where $A(\mathbf{k})$ is the aperture function (5.28). A graph of the ADF-STEM probe wave functions with Scherzer conditions is shown in Fig. 5.20 and 5.21. This is a complex valued function and the relative weighting of the real and imaginary parts can change dramatically with defocus etc.

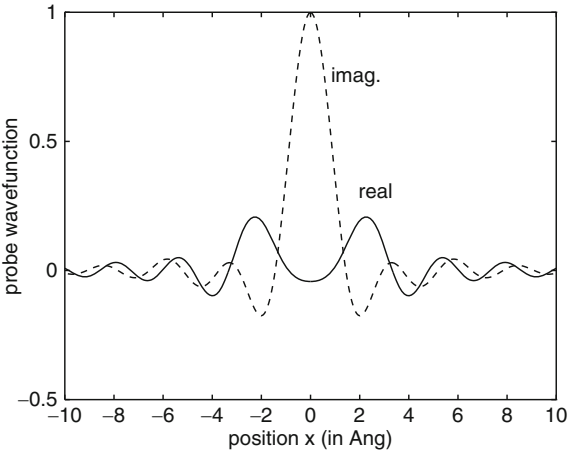

Fig. 5.20 Profile of the ADF-STEM probe wave functions (real and imaginary parts) for an electron energy of 200 keV, spherical aberration $C_s = 1.3$ mm., defocus $\Delta f = 700$Å, and an objective aperture of $\alpha_{\max} = 10.37$ mrad (Scherzer conditions). The effects of a finite source size have been ignored

The probe wave function is incident on the specimen and is modulated by the specimen transmission function $t(\mathbf{x})$ as it passes through the specimen. The wave function transmitted through the specimen is:

$$\begin{aligned}\psi_t(\mathbf{x},\mathbf{x}_p) &= \psi_p(\mathbf{x},\mathbf{x}_p)t(\mathbf{x}) \\ &= \psi_p(\mathbf{x},\mathbf{x}_p)\exp[i\sigma v_z(\mathbf{x})].\end{aligned} \tag{5.48}$$

In the STEM mode the transmitted wave function already has the effects of the objective lens aberration in it, unlike the CTEM mode where the objective lens effects enter after the wave function passes through the specimen. After passing through the specimen the transmitted wave function is then diffracted into the far field (i.e., the diffraction plane) and hits the ADF detector. Diffraction into the far field is equivalent to a Fourier transform of the transmitted wave function.

$$\Psi_t(\mathbf{k}) = \mathrm{FT}[\psi_t(\mathbf{x})]. \tag{5.49}$$

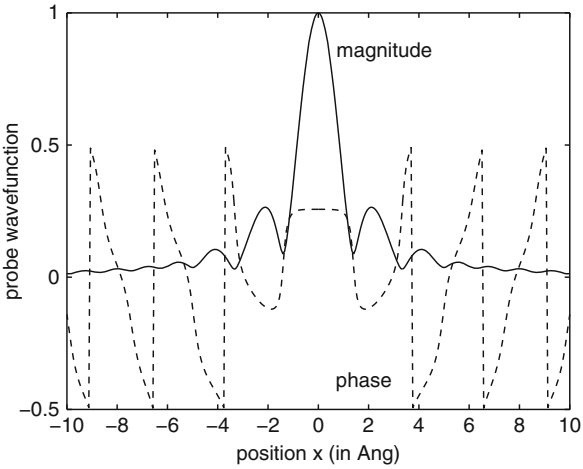

Fig. 5.21 Figure 5.20 replotted as a magnitude and phase. The phase is in units of 2π radians

The detector integrates the square modulus of the wave function in the diffraction plane to form the ADF-STEM signal at this point in the image (corresponding to the probe position $\mathbf{x}_p$):

$$g(\mathbf{x}_p) = \int D(\mathbf{k}) |\Psi_t(\mathbf{k}, \mathbf{x}_p)|^2 \mathrm{d}^2\mathbf{k}, \tag{5.50}$$

where $D(\mathbf{k})$ is the detector function:

$$\begin{aligned} D(\mathbf{k}) &= 1 \quad \text{on the detector} \\ &= 0 \quad \text{otherwise.} \end{aligned} \tag{5.51}$$

This process is repeated for each new position of the probe as it is scanned across the specimen (usually in a raster fashion). If $D(\mathbf{k})$ is a small point on the axis then the image is a bright field image and the discussion of Sect. 5.4 also applies via the reciprocity theorem. If the detector is a large annulus covering only high angle scattering then the image is an ADF (or annular dark field) image which is the focus of this section. This procedure is restated in algorithmic form in Table 5.3. The incoherent image model (3.66) captures many of the features of this calculation but is much faster (approximately as fast as the phase grating calculation) and may be a better approach in many cases.

5.5.1 Single Atom Images

The ADF detector in the STEM typically covers very large angles which will requires some changes to the sampling of the potential. First consider an image

Table 5.3 Steps in the calculation of STEM images of thin specimens

Step 1	Calculate the projected atomic potential $v_z(\mathbf{x})$ from (5.19) or (5.21).
Step 2	Calculate the transmission function $t(\mathbf{x}) = \exp[i\sigma v_z(\mathbf{x})]$ (5.25) and symmetrically bandwidth limit it.
Step 3	Calculate the probe wave function $\psi_p(\mathbf{x}, \mathbf{x}_p)$ at position $\mathbf{x}_p$ (5.45,5.47)
Step 4	Multiply the probe wave function by the specimen transmission function $t(\mathbf{x}) = \exp[i\sigma v_z(\mathbf{x})]$ to get the transmitted wave function $\psi_t(\mathbf{x})$.
Step 5	Fourier transform the transmitted wave function to get the wave function in the far field (diffraction plane).
Step 6	Integrate the intensity (square modulus) of the wave function in the diffraction plane including only those portions that fall on the annular detector (5.50). This is the signal for one point or pixel in the image.
Step 7	Repeat step 3 through step 6 for each position of the incident probe $\mathbf{x}_p$.

calculation of the five single atoms used in Fig. 5.13 for BF-CTEM phase contrast. The image is sampled in a 50Å by 50Å area. To get a scattering angle of 200 mrad at 200 keV requires that $0.5\lambda N_x/a \geq 200$ mrad. Therefore, the potential and wave functions should be sampled with 1024 pixels in each direction to get the large angles required for the ADF detector.

Figure 5.22 shows a line scan through the five single atoms used in Fig. 5.13. The transmission function (Fig. 5.11) is the same for both CTEM and STEM. The vertical axis is the portion of the incident probe intensity that falls on the ADF detector. The ADF signal (Fig. 5.22) is normalized slightly differently from the BF signal (Fig. 5.11) because of the different way in which they are generated. The ADF signal is relative to the total incident beam current but the BF signal is relative to the incident beam current density (the incident beam has a uniform intensity of one at all positions).

Even though the ADF signal and the BF signal are normalized differently it is apparent that the ADF signal is much weaker than the BF signal. However, the ADF signal shows a much stronger contrast between heavy and light atoms. It is even possible to image single heavy atoms on thin carbon supports many atoms thick because of the large increase in signal with atomic number Z (see for example Crewe et al. [68], Isaacson et al. [172] and Langmore et al. [222]). The peak single atom signal in ADF-STEM for all atoms is shown in Fig. 5.23 as a function of atomic number Z for three different electron beam energies. The ADF-STEM signal varies as approximately $Z^{1.5}$ to $Z^{1.7}$. Spherical aberration was fixed at $C_s = 1.3$ mm and Scherzer conditions were used for the defocus and the objective aperture. The inner angle of the ADF detector was set to four times the objective aperture and the outer angle was twenty times the objective aperture (this should integrate everything scattered beyond the inner angle). It is interesting to note that the single atom signal decreases with increasing electron beam energy contrary to BF phase contrast

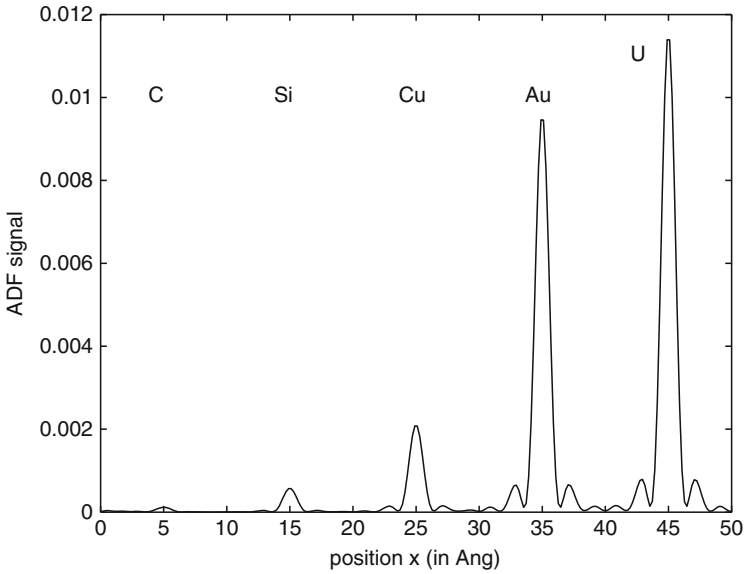

Fig. 5.22 Line scan of the ADF-STEM image intensity through the center of five isolated single atoms and an incident electron beam energy of 200 keV. The electron optical parameters are spherical aberration $C_s = 1.3$ mm, defocus $\Delta f = 700$ Å and an objective aperture of 10.37 mrad (Scherzer conditions). The ADF detector covers 40–200 mrad. This was calculated with a sampled image of 1024×1024 pixels (atomic number Z = 6,14,29,79,92)

signal shown in Fig. 5.14. As energy increases the resolution also increases meaning that the objective aperture also increases. The inner angle of the detector should be held at about 3–4 times the objective angle to remove any phase contrast effects. This means that the inner angle of the detector is also getting bigger so that there is less signal at high beam voltage (and higher resolution). The apparent signal decreases with increasing resolution in ADF-STEM. Also note that the weak phase object approximation may have small errors at 100 keV for very heavy atoms (Z near 100).

5.5.2 Thin Specimen Images

To simulate an image of (110) silicon also requires more sampling points than you might think at first. The image sequence given in Fig. 5.16 and 5.17 has a supercell size of $a \times b = 26.89 \times 27.15$ Å. The ADF-STEM detector collects large angles, and to get $\theta_d \sim 200$ mrad on the detector requires that the number of pixels in each direction be increased to about $N_x > 2a\theta_d/\lambda \sim 429$ pixels. The nearest power of 2 (for the FFT's) is 512×512 pixels.

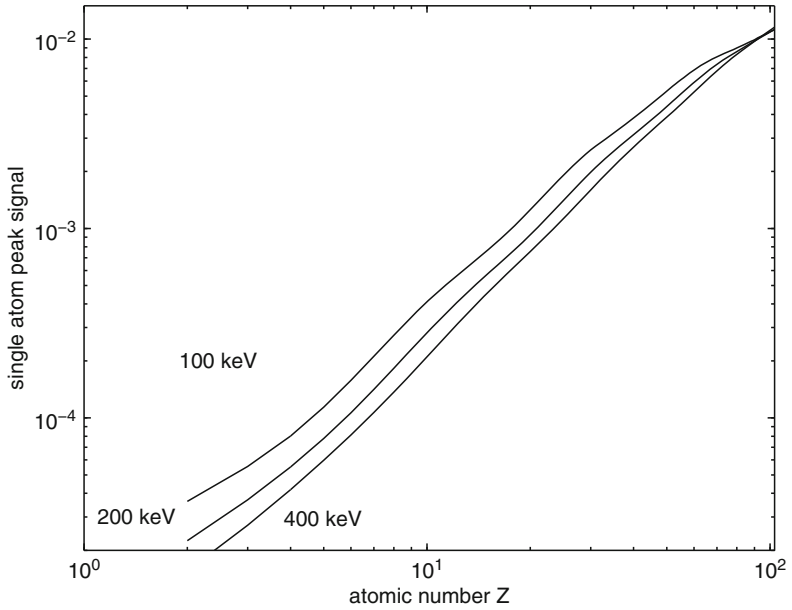

Fig. 5.23 Single atom peak signal in ADF-STEM vs. atomic number Z for 100 keV, 200 keV, and 400 keV. Spherical aberration was fixed at $C_s = 1.3$ mm and Scherzer conditions were used for defocus and objective aperture

Figure 5.24 shows the ADF-STEM image in the weak phase object approximation for three different energies (compare to Fig. 5.17). The specimen was four atoms thick and the signal is of the order of 10^{-3} to 10^{-4} of the incident beam intensity. The ADF detector spanned an angular range of 40–200 mrad for the 200 and 400 keV images and 45–200 mrad for the 100 keV image. The ADF signal with a large detector is an incoherent image mechanism and gives a slightly better resolution, however with a smaller signal. The characteristic dumb bell structure of silicon atom pairs (in the 110 projection) should be resolved at these beam energies and spherical aberration values. This ADF image does not rely on complicated scattering mechanisms like thermal diffuse scattering or high order Laue zones, but does qualitatively reproduce the features of an ADF-STEM image.

The simulated images in Fig. 5.24 are consistent with the incoherent annular dark field transfer functions as shown in Fig. 5.25. Both of the indicated spacings for the 110 projection of silicon can be resolved at the higher beam energies (compare to Fig. 5.25).

An experimental image of the 110 projection of silicon taken at 100 keV with an aberration corrected instrument is shown in Fig. 5.26. The dumbell spacing of 1.36Å is just barely resolved in this image. If only the geometrical lens aberration were considered for this image the probe size should be 1.0Å or less (and 1.36Å should be better resolved), however this image is most likely source limited.

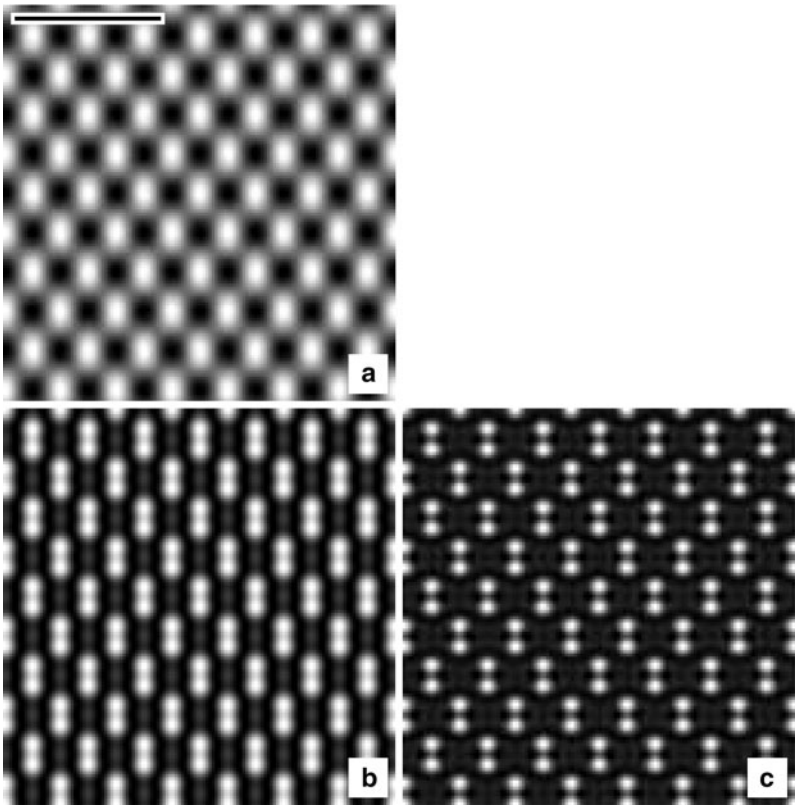

Fig. 5.24 Simulated ADF-STEM image of 110 silicon (4 atoms thick) in the weak phase object approximation with spherical aberration of $C_s = 1.3$ mm and three different beam energies. (a) 100 keV $\Delta f = 850$Å, $\alpha_{\max} = 11.4$ mrad. (b) 200 keV, $\Delta f = 700$Å, $\alpha_{\max} = 10.37$ mrad. (c) 400 keV, $\Delta f = 566$Å, $\alpha_{\max} = 9.33$ mrad. All are Scherzer conditions. The wave function was sampled with 512×512 pixels but the final image is calculated for 128×128 pixels. The scale bar in (a) is 10 Å. The image ranges are (a) 0.00033–0.00133, (b) 0.00018–0.00072 and (c) 0.00003–0.00039. White is a larger positive number. Atoms should appear white in both images

The tip was nearing the end of its life and probably produces a larger than normal source size (lower brightness). A sequence of images calculated in the simple incoherent image model (3.66) with different source sizes (3.74) is shown in Fig. 5.27. There is a reasonable match to image d) with a 1Å source size. This produces more beam current (good) but reduces the obtainable resolution (usually bad). Part of this apparent source size blurring is probably due to a small stage vibration of about 0.5Å which appears not to have a preferred direction. The higher the resolution the more severe are the requirements on instrumental stability of all types.

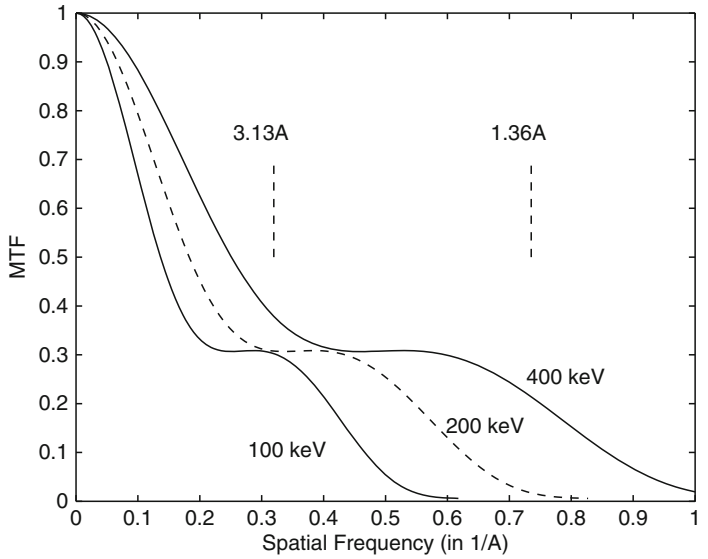

Fig. 5.25 The transfer function for an incoherent annular dark field STEM image in under Scherzer conditions. Spherical aberration is $C_s = 1.3$ mm and the electron energy varies from 100 kev to 400 keV. Two spacings relevant to the 110 projection of silicon are shown for comparison. About 1.36Å is the spacing between the dumbbells and 3.13Å is the spacing of the lowest order allowed reflection in the projected unit cell

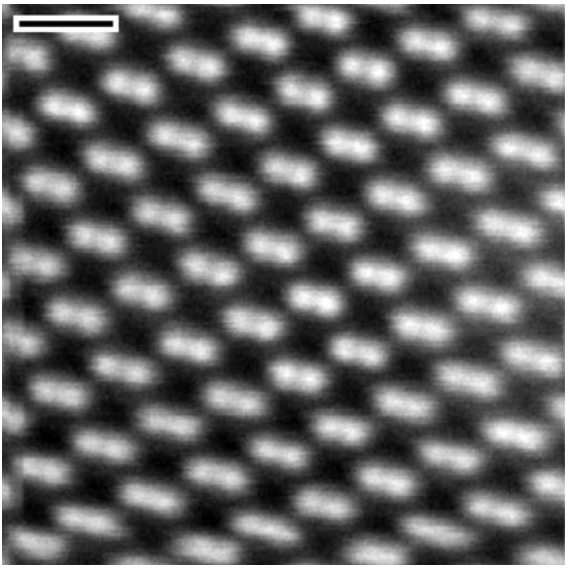

Fig. 5.26 Experimental ADF-STEM image of 110 silicon recorded on a NION Ultra-STEM at 100 keV (aberration corrected to third order with reduced fifth order) with 512×512 pixels and a 35 mrad objective aperture. The scale bar is 5 Å. Atoms should appear *white*. This image has been averaged over four frames and low pass filtered to a little above the instrumental resolution

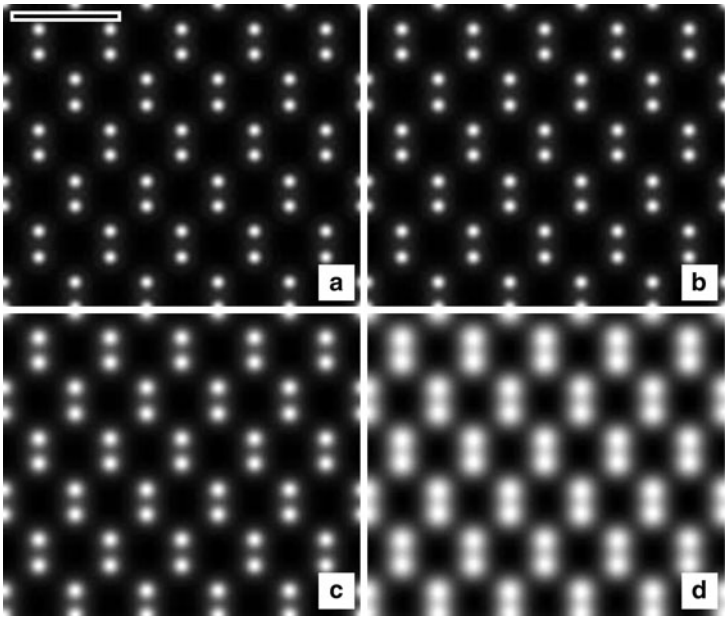

Fig. 5.27 Simple incoherent ADF-STEM images at 100 keV (C_{s3} =0 and C_{s5} = 5mm, 0 defocus and a 35 mrad obj. apert.). The scale bar is 5 Å. The source size is (a) 0.1Å, (b) 0.2Å, (c) 0.5Å, and (d) 1.0Å

5.6 Summary of Sampling Suggestions

The previous sections discussed sampling requirements for some specific cases in an anecdotal manner. There is really no easy way to calculate the required pixel size (sampling requirements) for every case in general. Usually you have to make an estimate of the sampling requirements, calculate an image with this estimate and compare to another calculation with better sampling (more and smaller pixels, etc.). If there is no significant change between the calculated images at two different pixels sizes (and number of pixels per image) then this is an indication that the image is correct. The deviation between two different calculations with different pixels sizes and number of pixels can also be used to estimate the error of the simulation itself. Table 5.4 gives a list of suggestions for the initial sampling sizes.

Table 5.4 Initial sampling suggestions for calculating images of thin specimens

1. The transmission function $t(\mathbf{x})$ (5.25) should be symmetrically bandwidth limited.
2. The real space pixel size Δx and Δy should be less than about $d_0/3$ to $d_0/4$ where d_0 is the resolution of the instrument.
3. The reciprocal space pixel size Δk_x and Δk_y should be less than about $k_{obj}/10$ where λk_{obj} is the maximum semiangle in the objective aperture.
4. The maximum angle in reciprocal space λk_{x-max} and λk_{y-max} should be about twice the maximum angle in the objective aperture (for CTEM) or slightly bigger than the maximum angle on the ADF-STEM detector (for STEM).